ROYAL SOCIETY OF CHEMISTRY

PAPER

Peeling from a liquid†

Deepak Kumar, [ID] *[a] Nuoya Zhou,[b] Fabian Brau, [ID] [c] Narayanan Menon [ID] [b] and Benny Davidovitch [ID] [b]

We establish the existence of a cusp in the curvature of a solid sheet at its contact with a liquid subphase. We study two configurations in floating sheets where the solid–vapor–liquid contact line is a straight line and a circle, respectively. In the former case, a rectangular sheet is lifted at its one edge, whereas in the latter a gas bubble is injected beneath a floating sheet. We show that in both geometries the derivative of the sheet's curvature is discontinuous. We demonstrate that the boundary condition at the contact is identical in these two geometries, even though the shape of the contact line and the stress distribution in the sheet are very different.

1 Introduction

The peel test is an extensively used method to measure the strength of adhesion of a sheet to a substrate. The test, schematically depicted in Fig. 1 panels A1–C1, is usually based on measuring the force required to separate the sheet from the substrate. A direct measurement of the shape of the sheet near the separation front, performed in a classic 1930 study by Obreimoff on freshly cleaved mica,[1] has been arguably the earliest attempt to determine the surface energy of solids. In this test, the peeled-off part of the sheet has a parabolic shape while the adhered portion of the sheet remains flat (Fig. 1B1). The discontinuity in curvature, $\kappa(s)$, where s is the distance to the contact line measured along the sheet profile, reflects a highly-localized torque (on the scale of the sheet's thickness) that is exerted by the rigid substrate on the peeled-off sheet. A localized torque is enabled by the rigidity of the substrate, which allows it to exert a highly-localized force oriented at an arbitrary angle to its surface. The presence of a singular torque underlies Obreimoff's law (see ESI†):

Peeling off rigid substrate:

$$[[k]] = \sqrt{2}/\ell_{bc} \qquad (1)$$

where:

$$\ell_{bc} \equiv \sqrt{B/T}. \qquad (2)$$

[a] *Department of Physics, Indian Insitute of Technology Delhi, New Delhi 110016, India. E-mail: krdeepak@physics.iitd.ac.in*
[b] *Department of Physics, University of Massachusetts Amherst, Amherst, MA 01003, USA*
[c] *Nonlinear Physical Chemistry Unit, Université libre de Bruxelles (ULB), CP231, 1050 Brussels, Belgium*
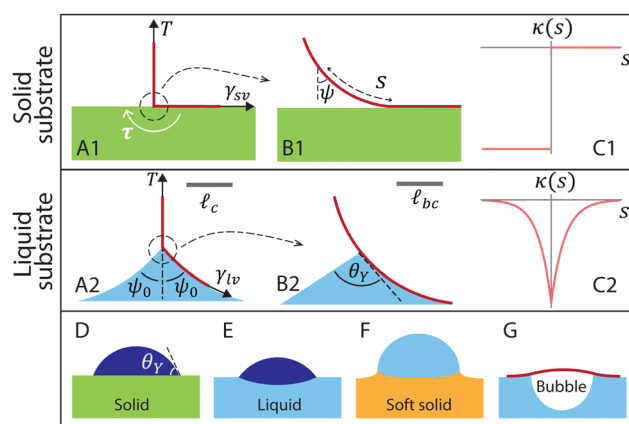† Electronic supplementary information (ESI) available. See DOI: https://doi.org/10.1039/d3sm00487b

Fig. 1 (A1) and (B1) Thin sheet peeling from a solid substrate (Obreimoff problem). s is the arc-length measured along the sheet from the contact line, such that s is positive in the adhered part of the sheet. ψ is the angle made by the tangent to the sheet with the vertical. (A2) and (B2) Thin sheet peeling from a liquid substrate (the problem studied in the current manuscript). Panels B1 and B2 are, respectively, zoomed-in versions of panels A1 and A2, at a bendo-capillary sale ℓ_{bc}. (C1) Curvature near the contact line for thin sheet peeling from a solid substrate[1] (corresponding to panels A1–B1). (C2) Continuous curvature for a thin sheet peeled from a liquid substrate characterized by a cusp at the contact line (corresponding to panels A2–B2). (D) Liquid drop on a rigid solid substrate (Young–Laplace–Dupree problem). (E) Liquid drop on a liquid substrate (Neumann problem). (F) Liquid drop on a soft solid substrate shows a wetting ridge near the contact line. We do not study this system here. (G) An air bubble under a thin sheet floating on a liquid substrate.

Here, $[[\kappa]] = \kappa(s \rightarrow 0^+) - \kappa(s \rightarrow 0^-)$ denotes the jump in curvature as a function of the coordinate s at the peeling front ($s = 0$) in the otherwise continuous curvature, B is the bending modulus of the sheet, and T is an adhesion energy (per area) of the solid,[2] which was attributed by Obreimoff to the surface energy of the solid with the ambient phase. In eqn (1), we follow

a terminology used in studies of elasto-capillary phenomena that involve slender bodies at fluid interfaces, where eqn (2) defines a "bendo-capillary" length, ℓ_{bc}, at which bending and tensile forces are comparable.

In this paper, we study peeling of a thin solid sheet from a liquid subphase, schematically depicted in Fig. 1 panels A2–C2. Our principal result is to establish, in two different experimental geometries, the boundary conditions that supplants the Obreimoff condition in this situation. In contrast to a rigid, solid subphase, the lack of shear rigidity of a liquid subphase removes the capability to generate a finite torque in an arbitrarily small vicinity of the contact line. This leads to two intimately-related differences from peeling off a rigid substrate. First, the liquid surface is deformed in a zone around the contact line, whose size is the capillary length (determined by the forces that restore flatness of interfaces, *i.e.* surface tension and gravity). Second, since it is not possible for a liquid subphase to apply a localized torque the curvature of the peeled-off sheet is continuous, and the only discontinuity at the contact line that is possible at mechanical equilibrium is of the derivative $\kappa'(s)$. The analogue of Obreimoff's law for peeling a solid sheet off a liquid subphase becomes:

peeling off liquid subphase:

$$[[\kappa]] = 0; \quad [[\kappa']] = \sin\theta_Y/\ell_{bc}^2, \tag{3}$$

where we again use the symbol $[[A]]$ for variations of $A(s)$ between the wet ($s > 0$) and dry ($s < 0$) parts of the solid sheet. Here, ℓ_{bc} is defined through eqn (2) with $T = \gamma_{\ell v}$, and

$$\theta_Y = \cos^{-1}[(\gamma_{sv} - \gamma_{s\ell})/\gamma_{\ell v}] \tag{4}$$

is the Young–Laplace–Dupré (YLD) angle, which is determined by the mutual surface energies between the liquid (ℓ), solid (s), and ambient vapor (v) phase. In ESI,† we use variational analysis to clarify the difference between peeling off a rigid substrate and a liquid sub-phase, eqn (1) and (3), respectively. While eqn (3) has been noted already in a one-dimensional (1D) model system of "bendable" partial wetting phenomena,[3] whereby a finite liquid volume is deformed upon making contact with a thin solid along a straight line,[4] our study is the first, to our knowledge, to confirm it experimentally. Another novelty of the current study is the implementation of these boundary conditions beyond the ideal 1D geometry assumed in ref. 3 and related works, to more-common 2D peeling geometries, where the stress distribution in the sheet is non-uniform and the contact line is curved. Determining a discontinuity in the derivative of the curvature (which amounts to the third derivative of a profile extracted from an image) is challenging, as noise-averaging smooths over the crucial localized feature we seek to identify. Indeed, we are not aware of any direct experimental study of a discontinuity in second derivative of the sheet profile in the solid-peeling case.

As illustrated in Fig. 1, the difference between the original Obreimoff law for peeling off a rigid substrate (eqn (1)) and its modified version for a liquid bath (eqn (3)), parallels the difference between the laws for a solid–liquid–vapor (YLD) and a liquid–liquid–vapor (Neumann) contact angle shown in Fig. 1D and E, respectively. There are two very common cases that deviate from the liquid (zero shear modulus) and rigid solid (infinite modulus) subphases presented in these two classic contact geometries. The first is to substitute the rigid solid by a soft, compliant elastic material as sketched in Fig. 1F. This has led to extensive studies of the so-called "wetting ridge"[5–8] that is produced at the three-phase contact line. In this paper, however, we study a less-explored, but quite common way (Fig. 1G) of introducing flexibility in the system by interposing a thin, bendable elastic sheet at the interface. Similarly to the difference between YLD contact (Fig. 1D) and Neumann contact (Fig. 1E), the difference between Obreimoff peeling problem (Fig. 1A1–C1) and peeling from a liquid subphase (Fig. 1A2–C2) stems from the fact that a liquid bath cannot support normal load without deforming its surface. However, in contrast to the contact angle problem on either a liquid or solid subphase (Fig. 1D and E), where the only length scale is the size of the liquid drop, the geometry of a sheet peeled-off from a liquid subphase involves multiple scales. Zooming in close to the contact line at a size scale $\ll \ell_{bc}$ (Fig. 1B2) reveals a geometry that is almost indistinguishable from the vicinity of a contact on a thick rigid body of the same material (Fig. 1D), except for a discontinuity of the 3rd derivative of the surface, which is reflected (Fig. 1C2) by a cusp in the curvature $\kappa(s)$. Zooming out (Fig. 1A2) to a size that is $\gg \ell_{bc}$ yet $\lesssim \ell_c = \sqrt{\gamma_{\ell v}/\rho g}$, the capillary length, one observes a liquid meniscus dominated by a balance of surface tension and gravity (Young–Laplace equation), which terminates at a kink, as if the curvature was diverging. This multi-scale scenario is valid only if the sheet is sufficiently thin, such that $\ell_{bc} \ll \ell_c$, or more generally:

$$\varepsilon \ll 1, \quad \text{where } \varepsilon \equiv (\ell_{bc}/L_{out})^2. \tag{5}$$

Here, L_{out} is an "outer" scale, at which the curvature approaches an asymptotic value, which is $\ll \ell_{bc}^{-1}$. For the example depicted in Fig. 1C2, where $L_{out} = \ell_c$, the ratio $\varepsilon = \rho g B/\gamma_{\ell v}^2$ is akin to the "softness" parameter that was defined in ref. 9.

2 1D translationally symmetric geometry

2.1 Theory

We first address an effectively one-dimensional geometry, where the deformed sheet is characterized by translational symmetry along the contact line, as shown schematically in Fig. 1A2 and 2A. Such a 1D set-up is realized in a floating, rectangular thin sheet, which is peeled off by exerting a vertical force T_{peel} along one of its short edges. As we noted above, when observed at intermediate scales, $|s| \gg \ell_{bc}$, the sheet appears to have a cusp at the contact line; furthermore, the mechanical equilibrium shape is characterized by reflection symmetry of the two sides of the surface (sheet-covered and liquid–vapor) around the vertical line as shown in ref. 11. The reflection
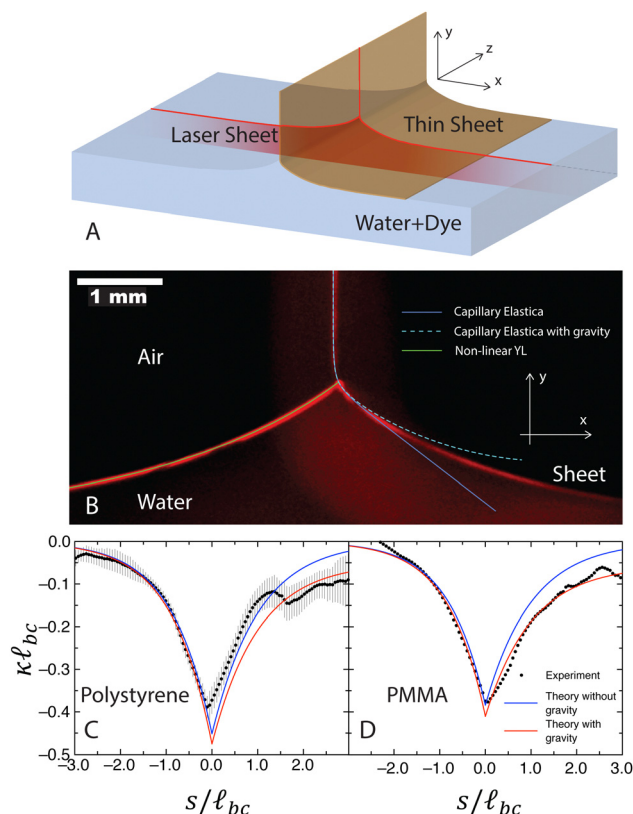
Fig. 2 1D geometry. (A) Schematic of experimental setup. The upper edge of the sheet is held at a fixed, controllable height. (B) A typical image of the sheet profile (polystyrene, thickness $t = 2$ μm corresponding to $\ell_{bc} = 0.2$ mm). Superimposed on the image are solutions of the non-linear Young–Laplace equation[10] (solid green line), the capillary elastica eqn (11) (solid blue curve), and the capillary elastica with gravity correction (dashed cyan curve). The curvature $\kappa(s)$ of the sheet for (C) polystyrene sheet ($t = 2$ μm) with estimated statistical error bars and (D) PMMA sheet ($t = 2$ μm). Filled black circles, blue and red lines represent data, theoretical prediction from capillary elastica, and capillary elastica with gravity correction, respectively. On the dry part ($s < 0$ in panels C and D, corresponding to the vertical segment in panels A and B), $\kappa(s)$ vanishes over a length ℓ_{bc}, whereas in the wet part ($s > 0$ in panels C and D, corresponding to the right part in panels A and B) $\kappa(s)$ reduces first to $\sim \ell_c^{-1}$ and vanishes only at a distance $\ell_c = \varepsilon^{-1/2}\ell_{bc} \gg \ell_{bc}$, from the contact line, due to the effect of liquid gravity.

symmetry indicates that the tension in the wet part of the sheet is identical to the liquid–vapor surface tension, $\gamma_{\ell v}$, and force balance at the contact line thus determines the force, T_{peel}, the opening angle, $2\psi_0$, of the apparent cusp, and the height, H_0, of the contact line over the liquid bath level:

$$T_{peel} = \gamma_{\ell v}(1 + \cos\theta_Y) = 2\gamma_{\ell v}\cos\psi_0 \qquad (6)$$

$$\Rightarrow \psi_0 \approx \cos^{-1}\left[\cos^2\frac{\theta_Y}{2}\right], H_0 \approx f(\psi_0)\ell_c, \qquad (7)$$

where the function $f(\psi_0)$ is found by solving the (nonlinear) Young–Laplace equation,[10] such that $f \approx (\pi/2 - \psi_0)$ for $\psi_0 \to \pi/2$ and $f \approx \sqrt{2}$ for $\psi_0 \to 0$. The shape of the whole sheet is described by a planar vector, $\vec{X}(s) = x(s)\hat{i} + y(s)\hat{j}$, where s is an arclength parameter, and is conveniently described through the angle, $\psi(s)$, between the tangent vector, $\vec{X}'$, and the downward vertical $-\hat{y}$:

$$x'(s) = \sin\psi; \; y'(s) = \cos\psi; \; \text{and } \kappa(s) = \psi'. \qquad (8)$$

At mechanical equilibrium, the shape satisfies the capillary elastica, which expresses normal force balance:[3,12]

$$B\left[\kappa'' + \frac{\kappa^3}{2}\right] - T(s)\kappa = -P(s) + \gamma_{\ell v}\sin\theta_Y\delta_d(s)$$

$$P(s) = \begin{cases} 0 & s < 0 \\ -\rho g y(s) & s > 0 \end{cases} \qquad T(s) = \begin{cases} T_{peel} & s < 0 \\ \gamma_{\ell v} & s > 0 \end{cases} \qquad (9)$$

where $s = 0$ is the position of the contact line, and $\delta_d(s)$ is the Dirac delta function. Here, $P(s)$ is the hydrostatic pressure exerted by the liquid bath on the wet portion of the sheet, $s > 0$, $T(s)$ is the tension in the sheet, and $\gamma_{\ell v}\sin\theta_Y$ is the normal force exerted by the liquid–vapor interface at the contact line. In a 1D geometry at mechanical equilibrium (and absence of external shear forces) the tension $T(s)$ satisfies $\partial_s T = 0$, and is consequently constant in the dry part ($s < 0$), where it is given by the force T_{peel} exerted by the peeler, and in the wet part ($s > 0$), where it is given by the liquid–vapor surface tension that pulls on the edge of the floating sheet.

Integrating both sides of eqn (9) over an infinitesimal neighborhood of the contact line, $s = 0$, we obtain:

$$B[[\kappa']] = \gamma_{\ell v}\sin\theta_Y \qquad (10)$$

and since the discontinuity of $\kappa'(s)$ is finite, integration of $\kappa'(s)$ across the contact line implies that $[[\kappa]] = 0$, thereby establishing eqn (3).‡

On each of the two portions of the sheet (dry, $s < 0$, and wet, $s > 0$), the profile is determined by the capillary elastica (9) which is a nonlinear 3rd order differential equation (ODE) for $\psi(s)$. Employing a common method for solving ODEs whose source term is localized ($\delta_d(s)$), we split the interval into two portions, $s > 0$ and $s < 0$, in each of which 3 boundary conditions (BCs) are required. Thus, a total of 6 independent BCs must be given, which characterize the behavior of the sheet at the dry and wet sides of the contact line, $s \to 0^+$ and $s \to 0^-$, respectively, as well as the dry and wet edges of the sheet. Eqn (3) comprise 2 of these BCs, hence 4 other BCs must be specified. To obtain them, we non-dimensionalize length by defining $\bar{s} = s/\ell_{bc}$ and $\bar{\kappa} = \kappa\ell_{bc}$, and consider the corresponding non-dimensionalized version of eqn (9), in the singular limit $\varepsilon \to 0$ (see ESI†). At $O(\varepsilon^0)$, we obtain 2 "outer" BCs at each side of the contact line. At $\bar{s} \to -\infty: \psi \to 0, \bar{\kappa} \to 0$, and at $\bar{s} \to +\infty:$ $\psi \to \psi_0, \bar{\kappa} \to 0$, and the corresponding (exact) solution of eqn (9) at $O(\varepsilon^0)$ is given by:

$$\bar{s} > 0: \bar{\kappa} = -2\,\text{sech}(\bar{s} + \bar{s}_w), \qquad (11)$$

---

‡ A higher-order effect, which cannot be accounted by eqn (9), is the small torque exerted by the liquid–vapor interface on the sheet if they are not perpendicular at the contact line (i.e. $\theta_Y \neq \pi/2$). This localized torque is explicitly proportional to the thickness, yielding a discontinuity of the curvature $[[\kappa']] \sim \cos(\theta_Y) \cdot t/\ell_{bc}^2$, whose effect on the shape is negligible, i.e. $[[\kappa']] \gg [[\kappa]]/\ell_{bc}$ for $t \ll \ell_{bc}$.

$$\bar{s} < 0: \bar{\kappa} = -2\sqrt{r}\,\mathrm{sech}[(\bar{s} + \bar{s}_{\mathrm{d}})\sqrt{r}],\ r \equiv \frac{T_{\mathrm{peel}}}{\gamma_{\ell v}} = 2\cos\psi_0,$$

where: $\quad \bar{s}_{\mathrm{w}} = \cosh^{-1}(a);\ \bar{s}_{\mathrm{d}} = -\cosh^{-1}(a\sqrt{r})/\sqrt{r};$

$$a = (2/\sin\theta_{\mathrm{Y}})\sqrt{b + \sqrt{b^2 - 1}};\ b = 1 + r. \qquad (12)$$

In the ESI,† we describe a next-order, $O(\varepsilon^1)$ solution, which incorporates the gravity effect on the sheet curvature and is useful for comparison with experimental data.

2.2 Experiment

The setup employed to study the 1D problem experimentally is illustrated schematically in Fig. 2A. Thin sheets of polystyrene (polymer source P10453-S, M_{w} = 97.6 kDa, Young's modulus = 3.5 GPa) and PMMA (Aldrich 182265, $M_{\mathrm{w}} \sim$ 996 kDa, Young's modulus = 3 GPa) of 1–2 μm thickness are prepared by spin-coating on glass slides. The choice of sheet thickness is restricted on one hand by the need to have an imaging resolution much smaller than ℓ_{bc} and on the other hand by the requirement that $\ell_{\mathrm{bc}} \ll \ell_{\mathrm{c}}$ for having a separation of scales as assumed in the theoretical analysis. Rectangles of 20 mm width and 60 mm length are cut from these films and floated on the surface of a water bath (ℓ_{c} = 2.7 mm). The sheets are floated from glass slides onto the water surface extremely slowly and carefully and we do not observe any air bubbles below the sheet. The long end of the film (along the z direction) is then lifted out of the water surface by using a triangular hanger made up of graphite rods of diameter 0.7 mm (pencil leads). A green laser sheet illumination (wavelength 532 nm) is used to illuminate the interface near the contact line for imaging. A dye (rhodamine-B) is dissolved in water in miniscule amount rendering both sides of the interface fluorescent. The interface is imaged using a DSLR camera (Nikon D5300) with a macro-lens and a long pass filter to admit only the fluorescent light. The laser sheet is positioned near the center of the film which is many ℓ_{c} away from the ends of the contact line. In this configuration end-effects, such as wrinkles seen near the edges of the sheet, are negligible and the film profile can be assumed to be 2D. A typical image obtained from the setup is shown in Fig. 2B. The resolution of the imaging setup (1 pixel $\sim$ 1 μm) is typically much smaller than ℓ_{bc}, which is approximately 0.2 mm for the sheets used. Superimposed on the image are the solution of the Young–Laplace equation[10] (green solid curve) for the liquid–vapor interface (left to the contact line), the solution to the capillary elastica without gravity as a blue solid curve, and the solution of the capillary elastica with gravity as the dashed cyan curve.

A gradient method is used to detect the interface and to obtain its (x, y) coordinates along the film from the images, and the curvature $\kappa(s)$ is computed from:

$$\kappa(x) = \frac{y''(x)}{(1 + y'(x)^2)^{3/2}};\ s(x) = \int_0^x \sqrt{1 + y'(x')^2}\,\mathrm{d}x', \qquad (13)$$

where $y(x)$ is the sheet profile measured from the image. On computing derivatives from experimental data, the noise

in the data gets amplified, which usually necessitates some form of smoothing. However, traditional smoothing methods will suppress any cusp in $\kappa(s)$. We therefore developed the algorithm described below to extract $\kappa(s)$ from the (x, y) data.

We divide the whole data set into intervals of length $\Delta \sim \ell_{\mathrm{bc}}$. Each of these intervals contains approximately 200 data points. We construct a sample of this data by choosing one data point from each interval randomly with a uniform probability distribution. We can estimate the position of the contact line from the images with a much higher accuracy and precision of a few pixels. We add to the data sample a contact-line location selected randomly with a Gaussian probability distribution centered at the estimated position of the contact line and having a width equal to the estimated error. A spline function of order 3 made up of Hermite polynomials is generated using this sampling of data points and the curvature is computed on this spline function at roughly every 10th point of the original data set. The process is repeated a large number of times (about twice the number of data points in each interval), selecting a different sampling of data points, such that the whole data set is adequately represented. The curvature profiles obtained from individual data samples are averaged to obtain the final $\kappa(s)$ curve. This procedure allows noise-averaging and use of the full data set without spatial averaging that would smooth the putative curvature cusp.

The black filled circles in Fig. 2C and D show $\kappa(s)$ as determined by the method described above, for a polystyrene (PS) and a PMMA film of thickness t = 2 μm, respectively. Superimposed on the experimental data are the theoretical predictions obtained by solving the capillary elastica equation neglecting gravity and capillary elastica with gravity in blue and red lines respectively. We notice that the theoretical predictions match the experimental data quite well and show a clear cusp at $s = 0$.

When gravity is neglected, the only input parameter required to solve the capillary elastica is ψ_0; however, this can be directly measured from the water–air interface near the contact line in the image and is found to be 48.8° and 40.0° for the PS and the PMMA films in Fig. 2C and D, respectively. In order to generate the solution of the capillary elastica with gravity, in addition to ψ_0, we need the value of $\varepsilon = (\ell_{\mathrm{bc}}/\ell_{\mathrm{c}})^2$, which is already known. Thus, there is no fitting parameter involved in computing the theory curves. The theoretical profiles calculated till order $O(\varepsilon^0)$ and $O(\varepsilon^1)$ match well with the experimentally measured sheet profile close to the contact line but deviate from it further away. These deviations are due to higher-order terms neglected in the calculation, which may become important far enough from the contact line.

3 Axial geometry

3.1 Theory

While the 1D geometry of the setup described in Fig. 2 presents a simple setting to discuss the boundary conditions at the contact line, the curvature cusp predicted by eqn (3) appears in

various other settings that are often encountered in elasto-capillary phenomena. One example is the axially-symmetric geometry of a thin sheet floating on water with an air-bubble of volume V underneath it, as shown schematically in Fig. 3A. In contrast to the 1D geometry, which is free of Gaussian curvature and whose mechanical equilibrium is thus described everywhere by a planar curve $\vec{X}(s)$ that solves the elastica, eqn (9), the axial geometry in Fig. 3 is characterized by Gaussian curvature, and thus involves a nontrivial variation of both radial and hoop components of the stress and curvature tensors with radial distance r. Hence, the shape of the sheet must be described by a surface $\vec{X}(r,\theta)$, that is obtained by solving the Föppl–von Kármán (FvK) equations,[13,14] and is furthermore susceptible to a radial wrinkling instability due to hoop compression exhibited by an axisymmetric solution.[15,16] Nevertheless, as long as the bendo-capillary length is sufficiently small, (namely, $\varepsilon \ll 1$, where L_{out} in eqn (5) is now given by the drop's radius and/or the capillary length ℓ_c), the dominant terms in the curvature and stress tensors in the vicinity of the contact line are the radial components, and consequently the normal force balance is given by an equation similar to eqn (9):

$$B\left(\kappa_\perp'' + \kappa_\perp^3/2\right) - \sigma_\perp \kappa_\perp = \gamma_{\ell v} \sin\theta_Y \delta_d(s), \qquad (14)$$

where $\kappa_\perp(s), \sigma_\perp(s)$ are principal components of the curvature and stress tensors, respectively, along the radial direction, perpendicular to the contact line, and s is the distance from the contact line. In the preceding analysis we neglected in

eqn (14) the sub-dominant hydrostatic pressure term; for similar reasons we ignore spatial variation of $\sigma_\perp$ on each side of the contact line. Once again, considering an infinitesimal vicinity of the contact line, we note that tangential force balance yields:

$$\sigma_\perp^{(d)} = \gamma_{\ell v} \cos\theta_Y + \sigma_\perp^{(w)} \qquad (15)$$

(where superscripts refer to the dry and wet sides), to which we refer as YLD equation, and integration of eqn (14) yields the jump condition, eqn (3).

The validity of eqn (14) hinges upon scale separation, namely $\varepsilon \ll 1$, where the ratio ε is given by eqn (5), with

$$\ell_{bc} \to \ell_{bc}^* \equiv \sqrt{B/\sigma_\perp}; \quad L_{out} \to \min\{\ell_C, V^{1/3}\} \qquad (16)$$

(see ESI† and ref. 14). Similarly to our analysis of eqn (9), the $O(\varepsilon^0)$ boundary conditions for eqn (14) consist of vanishing curvature away from the contact line (i.e. $\bar\kappa, \bar\kappa' \sim O(\varepsilon, \sqrt{\varepsilon})$, respectively). However, in contrast to the simpler 1D geometry, finding the asymptotic tangent angle $\psi_{1,2}$ at the two sides of the contact line, as well as the stress $\sigma_\perp$ in its vicinity, requires one to solve the FvK equations – a nonlinear set of partial differential equations – in the singular limit of vanishing bending rigidity (known as "membrane limit" or "tension field theory"). Rather than following such a theoretical track (see ref. 13 and 14), we note that force balance on an a box of intermediate size, $\ell_{bc}^* \ll \ell \ll L_{out}$, around the contact line (see Fig. 3B) implies that, at $O(\varepsilon^0)$:

$$\sigma_\perp^{(d)} = -\sigma_\perp^{(w)} \cos\psi_2 - \gamma_{\ell v} \cos(\psi_1 + \psi_2)$$
$$\sigma_\perp^{(w)} \sin\psi_2 = -\gamma_{\ell v} \sin(\psi_1 + \psi_2) \qquad (17)$$

(often called Neumann contact[17]), which implies that $\gamma_{\ell v}$ and the two asymptotic angles, ψ_1, ψ_2, uniquely determine the in-plane stress in the sheet, $\sigma_\perp^{(w)}$, $\sigma_\perp^{(d)}$, near the contact line, and consequently the YLD angle θ_Y by eqn (15). Note that for the 1D peeling geometry considered earlier, $\sigma_\perp^{(w)} = \gamma_{\ell v}$, whereas $\psi_1 = 2\psi_0$ and $\psi_2 = \pi - \psi_0$, such that eqn (15) and (17) reduce to eqn (6).

3.2 Experiment

The axial geometry is realised in the experiments by inserting an air bubble beneath a sheet floating on water using a syringe. To image the contact line between the bubble, sheet and water subphase, a vertical plane passing through the center of the setup is imaged using a laser-sheet fluorescence method similar to the one illustrated in Fig. 2A. A typical image of the sheet profile obtained from these experiments is shown in Fig. 3B. A bright-field image is taken after the fluorescence image, and used to obtain the profile of the air-bubble. The dashed white curve in Fig. 3B represents a circle fitted to the air-bubble shape. Fig. 3C and D show $\kappa(s)$ for bubble radii $R = 4.1$ mm and $R = 3.1$ mm, respectively. The data demonstrate that in this geometry too, the curvature has a cusp near $s = 0$, representing a discontinuity in the derivative of the curvature. Note that the curvature vanishes in the wet part ($s > 0, s \gg \ell_{bc}$), where the sheet is flat, and approaches a positive value in the dry part ($s < 0, |s| \gg \ell_{bc}$), where the air bubble imposes a curved shape on the sheet. Similarly to the effect of gravity in the 1D geometry,
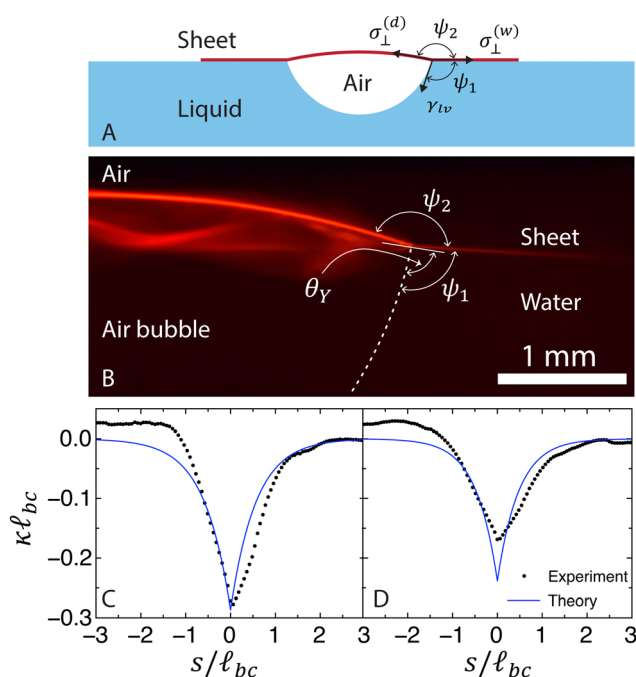

Fig. 3 2D axially-symmetric geometry. (A) The setup consists of a thin sheet floating on water with an air bubble underneath. (B) A typical image of the sheet profile (Polystyrene, thickness $t = 2$ μm). The dashed white curve is a circle fitted to the air bubble, and the white solid line is tangent to the sheet profile at the contact line. The curvature $\kappa(s)$ for air bubble of radius (C) 4.1 mm and (D) 3.1 mm.

this asymmetry of the asymptotic values of curvature is a higher order effect, which is not captured by a leading, $O(\varepsilon^0)$ analysis.

4 Discussion

Problems such as the 1D and axial peeling geometries in highly-bendable sheets typically come in two parts with a big separation in length scale – an "inner", bending-dominated region of size ℓ_{bc}^* that is governed by the elastica, and an "outer" region, where the shape and stress are independent of bending rigidity. At the innermost part of the bending-dominated zone is the purely local effect that we have established in this article, with a discontinuity in the gradient of the curvature in the vicinity of the contact line, $[[\kappa'_\perp]]$, which is determined purely by material parameters $(B, \gamma_{\ell v}, \theta_Y)$. This discontinuity affects the bending-dominated region as a "near-field" boundary condition to the elastica problem, but a complete solution of the elastica requires also a "far-field" boundary condition, which is obtained by matching with the outer, bending-independent problem. In the cases we considered, this matching condition is expressed through a single parameter, the asymptotic angle ψ_0 in Fig. 1 or equivalently $\psi_2 = \pi - \psi_0$ in Fig. 3. Neglecting the bending-dominated region altogether (as was proposed in ref. 18 for sufficiently thin sheets) leads to an error in the region close to the contact. Neglecting the curvature discontinuity at the contact line (as in the elastica problem for 1D delamination studied in ref. 19) can also lead to an error in the predicted shape, and when tension is small, the error may span a large portion of the sheet. We further note that the geometry-independent nature of the discontinuity, $[[\kappa'_\perp]]$, provides the basis for a robust method for determining contact angles both at and away from thermodynamic equilibrium.

In this work, we considered the peeling from a liquid substrate of an effectively inextensible, yet highly bendable solid sheet. In this case, any deformation of the sheet is described by the shape of its mid-surface, reflecting a balance of bending and interfacial forces, where the shape itself does not exhibit any irregularity up to a discontinuity of its 3rd derivative as is described in eqn (3). For a solid sheet of Young's modulus E and thickness t, such an effectively inextensible mechanics corresponds to the parameter regime $t \ll \ell_{bc}$, or equivalently $t \gg \ell_{ec}$, where $\ell_{ec} = \gamma/E$ is the "elasto-capillary" length (which inequality is additional to the inequality (5)). If one zooms in on a vicinity of size ℓ_{ec} of the contact line (assuming ℓ_{ec} is larger than the molecular scale of the solid phase), one may observe an actual cusp in the solid's surface, which is described by Neumann's law (see schematic Fig. 3a in ref. 20). If the solid sheet is made of sufficiently compliant material such that $t \gg \gamma/E$, the deformation of the sheet can no longer be described by the shape of its mid-surface, instead it must be considered as a 3D elastic body (similarly to Fig. 3b of ref. 20).

In conclusion, our study on the boundary condition of a liquid in contact with a bendable solid sheet brings closer to completion a glossary of elementary types of triple-phase contacts of solid and liquid bodies (Fig. 1D–G): starting from the classical Young–Laplace contact (1805) and Neumann contact (1894) to the Obreimoff contact (1930) and more recent studies on the wetting ridge formed by a liquid drop on a stretchable solid.[5–8]

Conflicts of interest

There are no conflicts to declare.

Acknowledgements

References

1 J. Obreimoff, *Proc. R. Soc. A*, 1930, **127**, 290–297.
2 C. Majidi, *Mech. Res. Commun.*, 2007, **34**, 85–90.
3 S. Neukirch, A. Antkowiak and J.-J. Marigo, *Proc. R. Soc. A*, 2013, **469**, 20130066.
4 C. Py, P. Reverdy, L. Doppler, J. Bico, B. Roman and C. N. Baroud, *Phys. Rev. Lett.*, 2007, **98**, 156103.
5 M. R. Shanahan and P.-G. De Gennes, *C. R. Acad. Sci., Paris B*, 1986, **302**, 517–521.
6 R. W. Style, R. Boltyanskiy, Y. Che, J. S. Wettlaufer, L. A. Wilen and E. R. Dufresne, *Phys. Rev. Lett.*, 2013, **110**, 066103.
7 S. J. Park, B. M. Weon, J. S. Lee, J. Lee, J. Kim and J. H. Je, *Nat. Commun.*, 2014, **5**, 4369.
8 B. Andreotti and J. H. Snoeijer, *Annu. Rev. Fluid Mech.*, 2020, **52**, 285–308.
9 J. Huang, B. Davidovitch, C. D. Santangelo, T. P. Russell and N. Menon, *Phys. Rev. Lett.*, 2010, **105**, 038302.
10 M. L. Anderson, A. P. Bassom and N. Fowkes, *Proc. R. Soc. A*, 2006, **462**, 3645–3656.
11 D. Kumar, T. P. Russell, B. Davidovitch and N. Menon, *Nat. Mater.*, 2020, **19**, 690–693.
12 G. Kozyreff, B. Davidovitch, S. G. Prasath, G. Palumbo and F. Brau, *Phys. Rev. E*, 2023, **107**, 035101.
13 R. Schroll, M. Adda-Bedia, E. Cerda, J. Huang, N. Menon, T. Russell, K. Toga, D. Vella and B. Davidovitch, *Phys. Rev. Lett.*, 2013, **111**, 014301.
14 B. Davidovitch and D. Vella, *Soft Matter*, 2018, **14**, 4913–4934.
15 J. Huang, M. Juszkiewicz, W. H. De Jeu, E. Cerda, T. Emrick, N. Menon and T. P. Russell, *Science*, 2007, **317**, 650–653.
16 B. Davidovitch, R. D. Schroll, D. Vella, M. Adda-Bedia and E. A. Cerda, *Proc. Natl. Acad. Sci. U. S. A.*, 2011, **108**, 18227–18232.
17 F. E. Neumann, *Theorie der Capillarität*, ed. A. Wangerin, Teubner Verlag, Leipzig, 1894.
18 T. Twohig, S. May and A. B. Croll, *Soft Matter*, 2018, **14**, 7492–7499.
19 T. J. Wagner and D. Vella, *Phys. Rev. Lett.*, 2011, **107**, 044301.
20 B. Andreotti and J. H. Snoeijer, *Europhys. Lett.*, 2016, **113**, 66001.